Applied Catalysis B: Environmental 101 (2011) 698–708

Contents lists available at ScienceDirect

Applied Catalysis B: Environmental

journal homepage: www.elsevier.com/locate/apcatb

Remarkable effect of the incorporation of titanium on the catalytic activity and SO_2 poisoning resistance of magnetic Mn–Fe spinel for elemental mercury capture

Shijian Yang[a], Yongfu Guo[a], Naiqiang Yan[a,*], Daqing Wu[b], Hongping He[b], Jiangkun Xie[a], Zan Qu[a], Jinping Jia[a]

[a] School of Environmental Science and Engineering, Shanghai Jiao Tong University, 800 Dong Chuan Road, Shanghai 200240, PR China
[b] Guangzhou Institute of Geochemistry, Chinese Academy of Sciences, 511 Kehua Street, Wushan, Tianhe District, Guangzhou 510640, PR China

ARTICLE INFO

Article history:
Received 9 July 2010
Received in revised form 2 November 2010
Accepted 5 November 2010
Available online 12 November 2010

Keywords:
Fe–Ti–Mn spinel
Elemental mercury
Capture capacity
Magnetic catalyst
SO_2 poisoning

ABSTRACT

Tiantium (Ti) was incorporated into non-stoichiometric Mn–Fe spinel to improve its performance for elemental mercury capture. Although the number of Mn^{4+} cations on $(Fe_2Ti_xMn_{1-x})_{1-\delta}O_4$ was less than that on the corresponding $(Fe_{3-x}Mn_x)_{1-\delta}O_4$, the number of usable cation vacancies for elemental mercury oxidization obviously increased. As a result, elemental mercury capture by Mn–Fe spinel was generally promoted by the incorporation of Ti. Furthermore, SO_2 mainly reacted with $\equiv Fe^{III}$–OH and few Mn^{4+} cations on the surface reacted with SO_2 at lower temperatures (100–150 °C), so SO_2 poisoning resistance improved at lower temperatures due to the incorporation of Ti. Especially, $(Fe_2Ti_{0.5}Mn_{0.5})_{1-\delta}O_4$ showed an excellent capacity (4.2 mg g^{-1}) for elemental mercury capture in the presence of a high concentration of SO_2 at 150 °C. Meanwhile, $(Fe_2Ti_{0.5}Mn_{0.5})_{1-\delta}O_4$ with the saturation magnetization of 30.6 emu g^{-1} can be readily separated from the fly ash using magnetic separation, leaving the fly ash essentially free of catalyst and adsorbed HgO. Therefore, nanosized $(Fe_2Ti_{0.5}Mn_{0.5})_{1-\delta}O_4$ may be a promising candidate catalyst for elemental mercury capture.

1. Introduction

Coal-fired utility boilers are currently the largest single-known source of anthropogenic mercury emissions. In China, approximately 38% of the emission of mercury comes from coal combustion [1]. In the United States, about one-third of the 150 tons of mercury emitted comes from coal-fired utility boilers [2]. In addition to particulate-bound mercury (Hg^p), elemental mercury (Hg^0) and oxidized mercury (Hg^{2+}) are also present as gaseous mercury in the flue gas from coal-fired utilities [3,4]. Particulate-bound mercury, which is associated with the fly ash, is effectively removed from the plant effluent by particulate control devices. Meanwhile, oxidized mercury is effectively removed from the flue gas by wet scrubbing or SO_2 control devices [3]. Because elemental mercury is not soluble in water, it is difficult to remove by currently available removal devices [5]. Therefore, elemental mercury is the major species emitted in the flue gas from coal-fired utilities [6]. In China, the total mercury concentrations in the flue gas from coal combustion boilers were in the range of 1.92–27.15 μg m^{-3}, with elemental mercury accounting for 66–94% of the total mercury and being the dominant species emitted to the atmosphere [7].

Many technologies have been investigated to remove elemental mercury from the flue gas, including sorbents, catalysts, and photochemical oxidations [8–21]. Catalysts for elemental mercury oxidization studied to date mainly fall into one of three groups: carbon-based catalysts (powdered activated carbon injection, PAC), selective catalytic reduction (SCR) catalysts, and metals and metal oxides [2]. The involved oxidants are mainly chlorine and oxygen. In China, the chlorine content in feed-coal varies from 63 to 318 mg kg^{-1}, which is much lower than the average value of US coals (628 mg kg^{-1}) [7], so catalytic oxidation of elemental mercury using gaseous oxygen in the flue gas as the oxidant is an economical method for elemental mercury control. Furthermore, the oxidized mercury formed (HgO or Hg_2O) is in a solid state at <300 °C, so it adsorbs on the catalyst and is then removed from the flue gas [22,23].

Mercury-catalyst materials are currently extremely restricted in their applications for at least four reasons: catalyst recovery, removal of toxin from industrial waste, interference of the chemical composition in the flue gas, and cost of operation [24]. First, the spent catalyst for this particular application is generally collected as a mixture with greater than 99% of ultrafine fly ash particles by

* Corresponding author. Tel.: +86 21 54745591; fax: +86 21 54745591.
E-mail addresses: yangshijiangsq@163.com (S. Yang), nqyan@sjtu.edu.cn (N. Yan).

0926-3373/$ – see front matter © 2010 Elsevier B.V. All rights reserved.
doi:10.1016/j.apcatb.2010.11.012

particulate control devices such as fabric filters or electrostatic precipitators (ESPs) [25]. It will be extremely difficult and impractical to reclaim the spent catalyst from the fly ash mixture for regeneration. Second, if the spent catalyst is not effectively removed from the fly ash mixture, the fly ash will be contaminated by mercury-loaded catalyst. If the contaminated fly ash is used as a cement additive, the toxin may be released in the cement plant during the calcination process. Third, the chemical composition in the flue gas (for example SO_2 and H_2O) may significantly affect elemental mercury oxidization by catalysts [17,18,26–29]. SO_2 gas molecules may compete with gaseous elemental mercury for the activity sites. The concentration of SO_2 in the real flue gas is about 10^4–10^5 times that of elemental mercury (v/v) [27,29]. Furthermore, SO_2 can react with metals and metal oxides to form a surface sulfate species [30,31], which may make them inefficient for elemental mercury oxidization. Fourth and mostly importantly, the catalyst must be cheap and easy to use.

The separation of catalyst from the fly ash can be solved by the magnetic property of catalyst material [24]. A magnetic sorbent MagZ-Ag^0 was once investigated for elemental mercury capture [25,32], but it was too expensive to apply in the larger coal-fired power plants. Previous researches have reported that maghemite (γ-Fe_2O_3) had some ability for elemental mercury oxidization [2,22]. γ-Fe_2O_3 is one of the simplest spinel ferrites. Spinel ferrites are of great fundamental and technological importance due to their structural, electronic, magnetic and catalytic properties [33]. Furthermore, an interesting feature of spinel ferrites is the possibility to replace iron cations by other metal cations while maintaining the spinel structure [34]. The physicochemical properties of spinel ferrites are strongly dependent on the site, nature and amount of metal incorporated into the structure. Ti^{4+} in the γ-Fe_2O_3 structure can strongly improve the ability for elemental mercury oxidization, but the presence of a high concentration of SO_2 can result in a severe interference. Furthermore, the incorporation of Mn^{4+} into the γ-Fe_2O_3 structure to form non-stoichiometric Mn–Fe spinel can promote elemental mercury oxidization, but a high concentration of SO_2 still shows a moderate negative effect.

Previous researches demonstrated that Fe–Ti–Mn mixed oxides showed a promising application in environmental catalysis [35–39]. Here, titanium was incorporated into the structure of non-stoichiometric Mn–Fe spinel to improve its catalytic ability for elemental mercury oxidation and to suppress the interference of a high concentration of SO_2. A series of $(Fe_2Ti_xMn_{1-x})_{1-\delta}O_4$ were synthesized using a co-precipitation method and characterized using X-ray diffraction (XRD), N_2 adsorption/desorption isotherms, transmission electron microscopy (TEM), X-ray photoelectron spectroscopy (XPS) and magnetization measurement. Then, a packed-bed reactor system was used to preliminarily evaluate their performance for elemental mercury capture.

2. Experimental

2.1. Sample preparation

Nanosized $Fe_2Ti_xMn_{1-x}O_4$ was prepared using a co-precipitation method. Suitable amounts of titanium tetrachloride, ferrous sulfate, ferric trichloride, and manganous sulfate were dissolved in distilled water (cation concentrations $\approx 0.3\ mol\ L^{-1}$).

This mixture was added to an ammonium hydroxide solution leading to an instantaneous precipitation according to the following reaction:

$$(2-2x)Fe^{3+} + 2xFe^{2+} + xTi^{4+} + 8OH^- + (1-x)Mn^{2+} \rightarrow Fe_2Ti_xMn_{1-x}O_4 + 4H_2O \quad (1)$$

During the reaction, the system was continuously stirred at 800 rpm. According to Ti, Mn and Fe solubility constants, the precipitate composition was the same as it in the liquid phase. The particles were then separated by centrifugation at 4500 rpm for 5 min and washed with distilled water. After 3 washings, the particles were collected and dried in a vacuum oven at 105 °C for 12 h. After the thermal treatment at 400 °C under air for 3 h, $(Fe_2Ti_xMn_{1-x})_{1-\delta}O_4$ was obtained according to the following reaction:

$$(1-\delta)Fe_2Ti_xMn_{1-x}O_4 + 2\delta O_2 \rightarrow (Fe_2Ti_xMn_{1-x})_{1-\delta}\square_{3\delta}O_4 \quad (2)$$

$(Fe_2Ti_xMn_{1-x})_{1-\delta}O_4$ had a structure similar to that of $Fe_2Ti_xMn_{1-x}O_4$. It differed from $Fe_2Ti_xMn_{1-x}O_4$ in that all of the Fe cations were in the trivalent state and most of the Mn cations were in the trivalent/tetravalent state. Meanwhile, cation vacancies (□) were incorporated to compensate for the oxidation of Fe^{2+} and Mn^{2+} [34]. With the increase of Ti content (i.e. x) in $Fe_2Ti_xMn_{1-x}O_4$, the amount of Fe^{2+} obviously increased and the amount of Mn^{2+} decreased (shown in Reaction (1)). As a result, the cation vacancies in $(Fe_2Ti_xMn_{1-x})_{1-\delta}O_4$ resulting from the oxidation of Fe^{2+} obviously increased with the increase of Ti content.

Furthermore, Ni was incorporated into the structure of Mn–Fe spinel as a comparison.

2.2. Sample characterization

Crystal structure was determined using an X-ray diffractionmeter (BRUKER-AXS) between 20° and 70° at a step of $2°\ min^{-1}$ operating at 35 kV and 30 mA using Cu Kα radiation. BET surface area was determined using a nitrogen adsorption apparatus (Micromeritics ASAP 2010 M+C). The sample was outgassed at 200 °C before BET measurement. Saturation magnetization was determined using a vibrating sample magnetometer (VSM, Model JDM-13) at room temperature. TEM image was performed on a JEOL JEM-2010 TEM. The micrographs were obtained in the bright-field imaging mode at an acceleration voltage of 200 kV. XPS (Thermo ESCALAB 250) was used to determine the binding energies of Fe 2p, Mn 2p, Ti 2p, S 2p, O 1s and Hg 4f with Al Kα ($h\nu$ = 1486.6 eV) as the excitation source. The C 1s line at 284.6 eV was taken as a reference for the binding energy calibration.

2.3. Elemental mercury capture

The assembly used for elemental mercury capture consisted of an elemental mercury permeation tube, a packed-bed reactor, a cold vapor atomic absorption spectrometer (CVAAS) and an online data acquisition system (shown in Fig. 1). A flow of air passed through the permeation tube and yielded a stable concentration of elemental mercury. A temperature control device was employed to keep the reactor at the desired temperatures. The gas containing elemental mercury first passed through the empty tube, and then entered the CVAAS to determine the baseline. When the concentration of elemental mercury had fluctuated within ±10% for more than 30 min, the gas was diverted to the catalyst bed for the test. An exact amount of catalyst was inserted in the middle of the column reactor and then packed with quartz wool to support the catalyst layer and avoid its loss. It was demonstrated that quartz wool has no ability for elemental mercury capture.

To preliminarily estimate the performance for elemental mercury capture, $(Fe_2Ti_xMn_{1-x})_{1-\delta}O_4$ was first tested under air. The inlet gas contained about $1.30\ mg\ Nm^{-3}$ (±20%) of elemental mercury and 20–30 $g\ Nm^{-3}$ of H_2O (uncontrolled) with a feed of $12\ L\ h^{-1}$. For each test, the time was about 10 h, the catalyst mass was 30.0 mg (the gas space velocity was about $1.2 \times 10^6\ h^{-1}$) and the reaction temperatures varied from 100 to 400 °C.

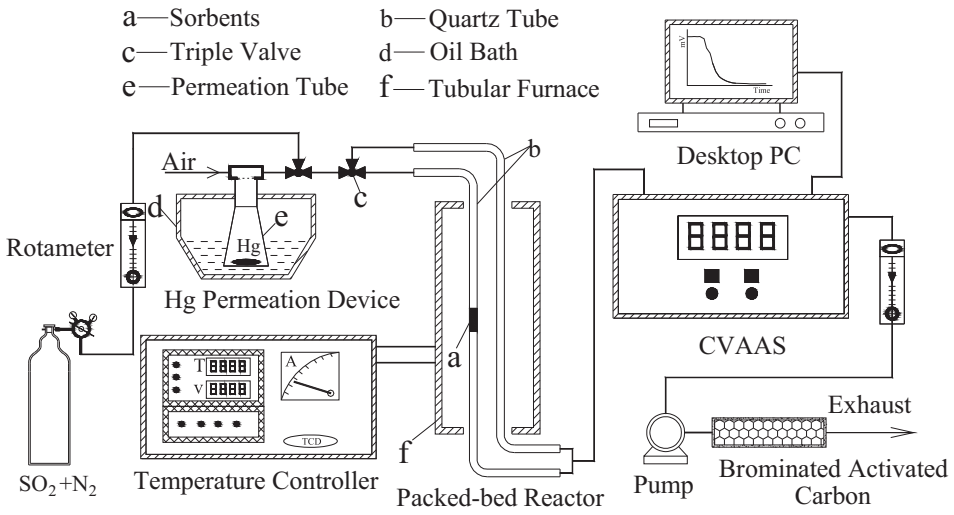

Fig. 1. Experimental system for packed-bed test.

Next, the effect of a high concentration of SO_2 on elemental mercury capture was investigated. The gas contained about 1.30 mg Nm^{-3} (±20%) of elemental mercury, 2.8 g Nm^{-3} of SO_2, 20–30 g Nm^{-3} of H_2O (uncontrolled) and 10% of O_2 with a feed of 12 L h^{-1}.

The concentration of elemental mercury in the gas was analyzed using an SG-921 CVAAS. Meanwhile, the concentration of Hg^{2+} at the exit of the reactor was determined using the Ontario Hydro Method (OHM) [7]. The breakthrough curve was generated by plotting the CVAAS voltage signal.

3. Results and discussion

3.1. Sample characterization

3.1.1. XRD

XRD patterns of synthesized samples are shown in Fig. 2. The characteristic reflections of $(Fe_2Ti_{0.8}Mn_{0.2})_{1-\delta}O_4$ and $(Fe_2Ti_{0.5}Mn_{0.5})_{1-\delta}O_4$ corresponded very well to the standard card of maghemite (JCPDS: 39-1346). Additional reflections that would indicate the presence of other crystalline manganese and titanium oxides, such as rutile, anatase, Mn_3O_4 (hausmannite), Mn_2O_3 (bixbyite) or MnO_2, did not present in the diffraction scan. This indicates that both Mn and Ti were incorporated into the spinel structure. In addition to the reflections corresponding to the spinel, a subtle reflection centered at 33.32° appeared in the XRD pattern of $(Fe_2Ti_{0.3}Mn_{0.7})_{1-\delta}O_4$, which was ascribed to $(Fe,Mn)_2O_3$ (bixbyite).

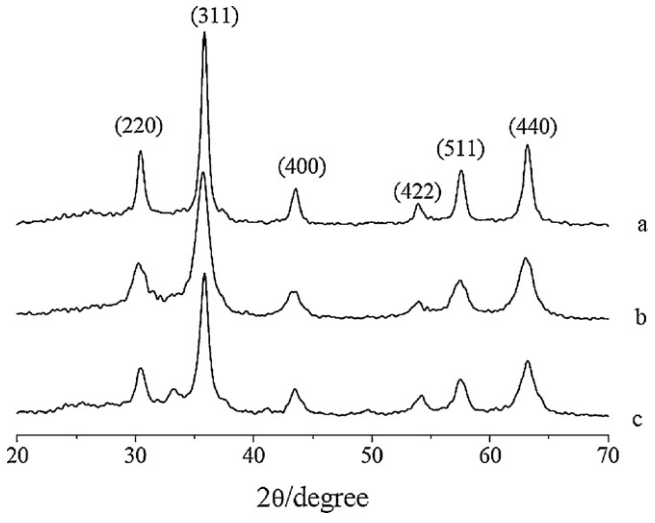

Fig. 2. XRD patterns of synthesized: (a) $(Fe_2Ti_{0.8}Mn_{0.2})_{1-\delta}O_4$; (b) $(Fe_2Ti_{0.5}Mn_{0.5})_{1-\delta}O_4$; (c) $(Fe_2Ti_{0.3}Mn_{0.7})_{1-\delta}O_4$.

Crystal sizes of synthetic samples were calculated with Scherrer's equation [40] (shown in Table 1).

3.1.2. TEM

The TEM images (Fig. 3) reveal irregular agglomerated nanoparticles of Fe–Ti–Mn oxide (darker contrast in the figures). As shown in Fig. 3, the particle size of $(Fe_2Ti_{0.5}Mn_{0.5})_{1-\delta}O_4$ was much smaller than those of $(Fe_2Ti_{0.8}Mn_{0.2})_{1-\delta}O_4$ and $(Fe_2Ti_{0.3}Mn_{0.7})_{1-\delta}O_4$. This result was consistent with the observation of BET surface area and the result of XRD analysis (shown in Table 1). It is worth mentioning that each particle was probably composed of a mono-crystal, since the crystal sizes obtained from XRD analysis were close to the particle sizes in the TEM images. As shown in Fig. 3c, the formed bixbyite rod can be observed, which was consistent with the result of XRD analysis.

Supplementary information was obtained from selected area electron diffraction patterns (SAED). All samples showed obvious diffuse diffraction rings, as a consequence of the small crystallites, that can be ascribed to the reflections of (2 0 0), (3 1 1), (4 0 0), (5 1 1) and (4 4 0) crystallographic planes of a cubic spinel phase.

3.1.3. Magnetization

A particular feature of the catalyst is its magnetic property, which makes it possible to separate the catalyst from the fly ash. Saturation magnetization of synthesized $(Fe_2Ti_xMn_{1-x})_{1-\delta}O_4$ is shown in Table 1. As shown in Fig. 4, $(Fe_2Ti_{0.5}Mn_{0.5})_{1-\delta}O_4$ showed the super-paramagnetism with a minimized coercivity and a negligible magnetization hysteresis.

Table 1
Crystal size, BET surface and saturation magnetization of synthesized samples.

	Crystal size (nm)	BET surface area (m^2 g^{-1})	Saturation magnetization (emu g^{-1})
$(Fe_2Ti_{0.8}Mn_{0.2})_{1-\delta}O_4$	16	56.4	34.4
$(Fe_2Ti_{0.5}Mn_{0.5})_{1-\delta}O_4$	11	107	30.6
$(Fe_2Ti_{0.3}Mn_{0.7})_{1-\delta}O_4$	13	52.0	28.9

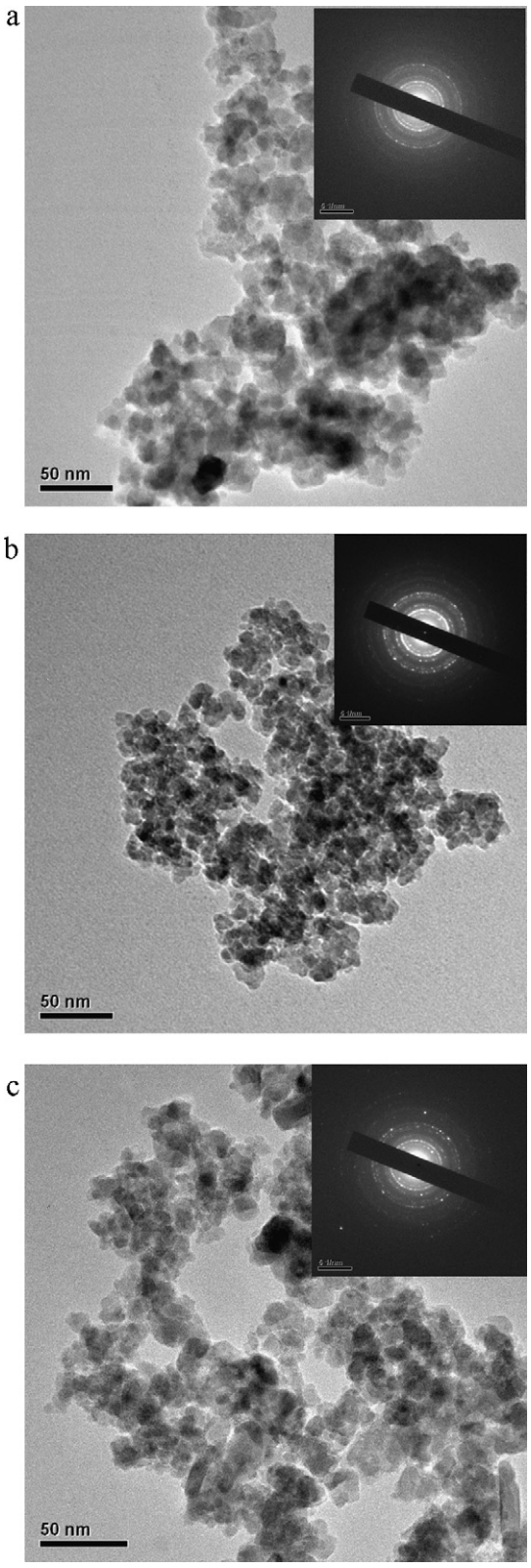

Fig. 3. TEM images of synthesized: (a) $(Fe_2Ti_{0.8}Mn_{0.2})_{1-\delta}O_4$; (b) $(Fe_2Ti_{0.5}Mn_{0.5})_{1-\delta}O_4$; (c) $(Fe_2Ti_{0.3}Mn_{0.7})_{1-\delta}O_4$.

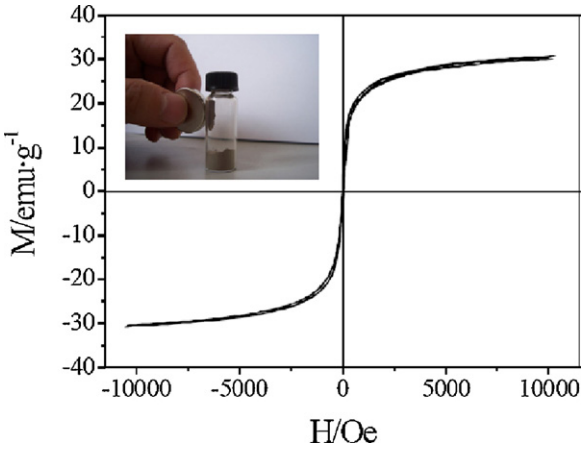

Fig. 4. Magnetization characteristics of synthesized $(Fe_2Ti_{0.5}Mn_{0.5})_{1-\delta}O_4$. The insert shows the result of separating $(Fe_2Ti_{0.5}Mn_{0.5})_{1-\delta}O_4$ from the fly ash.

The magnetic catalysts can be recovered in situ by a two-step process. Particulates can first be removed from the flue gas by an ESP, followed by the magnetic separation of the catalyst and adsorbed mercury from the fly ash. Previous research had demonstrated that the magnetic sorbent MagZ-Ag^0 can be easily separated from the fly ash [25,32]. The photograph inserted in Fig. 4 shows the result of separating $(Fe_2Ti_{0.5}Mn_{0.5})_{1-\delta}O_4$ from the mixture with 10 g of fly ash and 1 g of $(Fe_2Ti_{0.5}Mn_{0.5})_{1-\delta}O_4$ by a normal magnet. After $(Fe_2Ti_{0.5}Mn_{0.5})_{1-\delta}O_4$ was separated from the mixture, the contents of Mn and Fe in the fly ash did not increase. This demonstrates that $(Fe_2Ti_{0.5}Mn_{0.5})_{1-\delta}O_4$ can be readily separated from the fly ash using magnetic separation, leaving the fly ash essentially free of catalysts and adsorbed mercury. However the mass of $(Fe_2Ti_{0.5}Mn_{0.5})_{1-\delta}O_4$ increased because some fly ash adsorbed on it.

3.1.4. XPS

Surface information on synthesized samples was analyzed by XPS. XPS spectra over the spectral regions of Fe 2p, Mn 2p, Ti 2p and O 1s were evaluated. XPS spectra over the spectral regions of Fe 2p and Mn 2p are shown in Fig. 5.

The O 1s peaks mainly centered at about 529.9 eV, as expected for transition metal oxides. Another oxygen species centered at about 531.4 eV was also observed, which was assigned to hydroxyl group (–OH) [41,42]. The Ti peaks were assigned to Ti $2p_{1/2}$ (464.0 eV) and Ti $2p_{3/2}$ (458.3 eV) of Ti^{4+}.

The Fe peaks were assigned to oxidized Fe species, more likely Fe^{3+} type species [41,42]. The binding energies centered at about 710.0 and 711.3 eV may be assigned to Fe^{3+} cations in the spinel structure, and the binding energy centered at about 712.4 eV was ascribed to Fe^{3+} bonded with hydroxyl groups ($\equiv Fe^{III}$–OH). This assignment was supported by the satellite component observed at about 719 eV, which is the fingerprint of the Fe^{3+} species [41].

The Mn peaks were assigned to Mn^{2+} (640.4 eV), Mn^{3+} (641.4 eV) and Mn^{4+} (642.4 eV). The ratios of Mn, Fe, Ti and O species on $(Fe_2Ti_xMn_{1-x})_{1-\delta}O_4$ collected from XPS analysis are shown in Table 2. There were few Mn^{2+} cations on $(Fe_{2.5}Mn_{0.5})_{1-\delta}O_4$ and $(Fe_{2.2}Mn_{0.8})_{1-\delta}O_4$ (shown in Table 2), so the presence of Mn^{2+} cations on $(Fe_2Ti_{0.5}Mn_{0.5})_{1-\delta}O_4$ and $(Fe_2Ti_{0.3}Mn_{0.7})_{1-\delta}O_4$ may result from the incorporation of Ti. Previous researches on Mn–Fe spinel [43] and Cu–Fe–Mn spinel [44] reported that Mn^{4+} cations preferred to be reduced to Mn^{3+} cations to form bixbyite at higher temperatures (>400 °C). Thus, some Mn^{4+} cations on $(Fe_2Ti_xMn_{1-x})_{1-\delta}O_4$ may be reduced to Mn^{2+} cations at higher temperatures to sustain the spinel structure due to the stabilization effect of Ti^{4+} cations on the spinel structure [40].

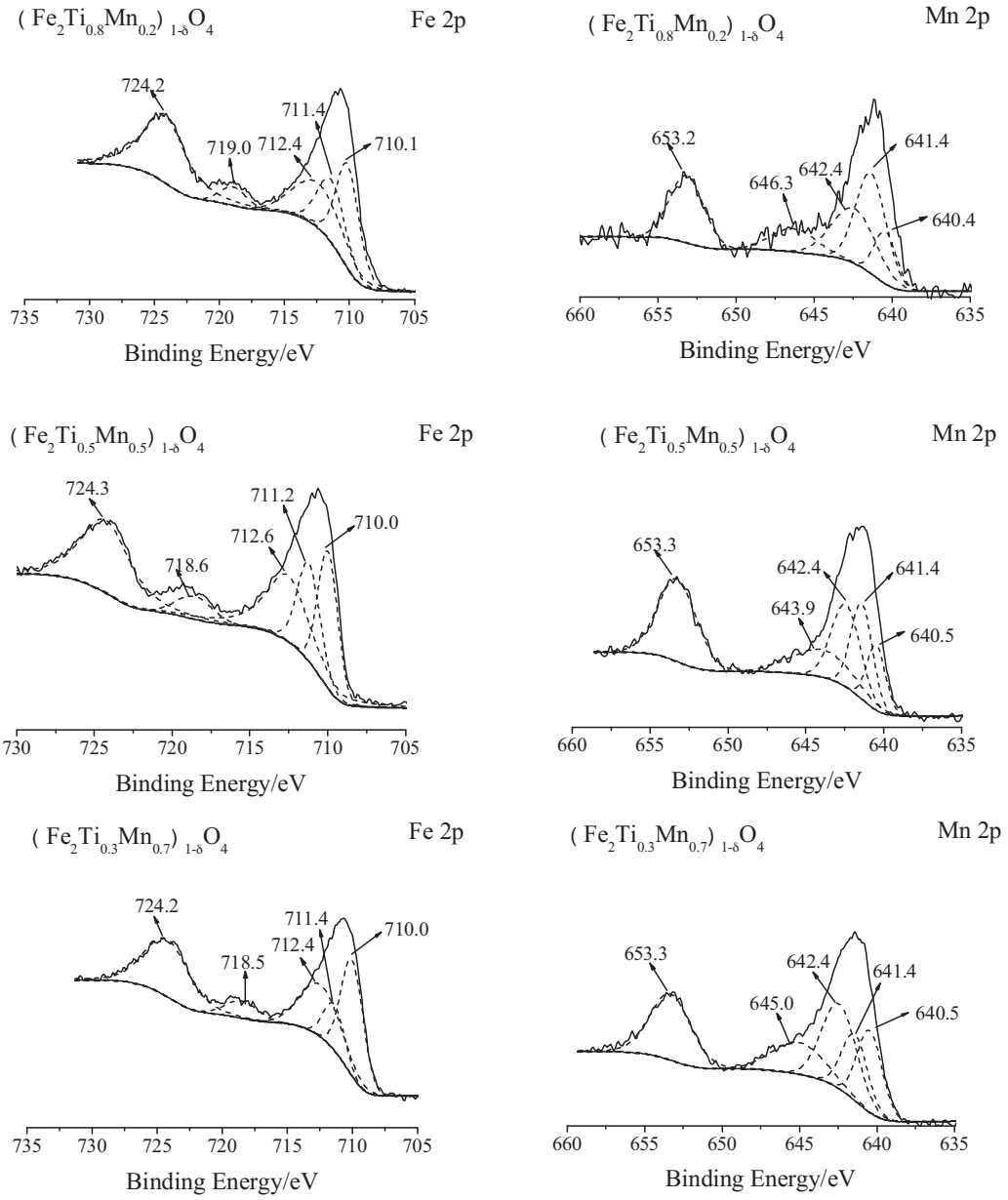

Fig. 5. XPS spectra of synthesized samples over the spectral regions of Fe 2p and Mn 2p.

Table 2 shows that the chemical heterogeneity (i.e. an enrichment of Mn cations on the surface) happened in the non-stoichiometric Mn–Fe spinel. Chemical heterogeneity can be studied by comparing average chemical composition with surface chemical composition (i.e. Mn/Ti + Fe + Mn) [45]. As shown in Table 2, the chemical heterogeneity was suppressed due to the incorporation of Ti or Ni into the Mn–Fe spinel structure.

3.2. Elemental mercury capture under air

3.2.1. Performance for elemental mercury capture

The determination of Hg^{2+} concentration at the exit of reactor showed that there was little Hg^{2+} in the gas after passing through the reactor tube with the catalyst, so the reduced amount of elemental mercury in the breakthrough curve was captured

Table 2
Data of atomic ratios collected from XPS%.

	O	Fe	Fe^{3+}	$\equiv Fe^{III}$–OH	Ti/Ni	Mn	Mn^{2+}	Mn^{3+}	Mn^{4+}	Mn/Fe + Mn + Ti on the surface	Mn/Fe + Mn + Ti in the structure
$(Fe_2Ti_{0.8}Mn_{0.2})_{1-\delta}O_4$	61.8	23.6	15.6	8.0	10.5	4.4	0.7	2.0	1.7	11	7
$(Fe_2Ti_{0.5}Mn_{0.5})_{1-\delta}O_4$	61.4	26.0	15.1	10.9	5.0	7.8	1.7	2.9	3.2	20	17
$(Fe_2Ti_{0.3}Mn_{0.7})_{1-\delta}O_4$	61.3	24.2	15.0	9.2	3.6	11.1	3.3	2.9	5.0	29	23
$(Fe_2Ni_{0.2}Mn_{0.8})_{1-\delta}O_4$	60.5	24.6	13.3	11.3	3.9	11.3	–	6.0	5.3	28	27
$(Fe_{2.2}Mn_{0.8})_{1-\delta}O_4$	61.3	20.3	12.6	7.7	–	18.5	–	7.2	11.3	48	27
$(Fe_{2.5}Mn_{0.5})_{1-\delta}O_4$	59.7	26.7	16.3	10.4	–	13.6	–	7.6	6.0	34	23
$(Fe_{2.8}Mn_{0.2})_{1-\delta}O_4$	59.7	35.3	25.4	9.9	–	5.1	3.0	–	2.1	13	7

Table 3
Capacity (Q) and breakthrough ratio (η) of synthesized samples for elemental mercury capture under air (mg g^{-1}).

		100 °C	150 °C	200 °C	250 °C	300 °C	350 °C	400 °C
$(Fe_{2.7}Ti_{0.3})_{1-\delta}O_4$	Q	<0.3	<0.3	0.48	0.76	0.58	0.48	0.40
	η	>90%	>90%	>90%	85%	84%	>90%	>90%
$(Fe_{2.2}Ti_{0.8})_{1-\delta}O_4$	Q	<0.3	<0.3	1.14	2.18	1.20	0.70	0.60
	η	>90%	>90%	>90%	83%	>90%	>90%	>90%
$(Fe_2Ti)_{1-\delta}O_4$	Q	<0.3	<0.3	1.54	3.94	3.44	1.62	1.38
	η	>90%	>90%	88%	23%	33%	66%	>90%
$(Fe_{2.8}Mn_{0.2})_{1-\delta}O_4$	Q	1.92	1.80	1.60	2.20	0.84	<0.3	<0.3
	η	62%	71%	89%	71%	84%	>90%	>90%
$(Fe_{2.5}Mn_{0.5})_{1-\delta}O_4$	Q	2.90	2.92	2.42	3.71	1.74	<0.3	<0.3
	η	48%	45%	61%	30%	70%	>90%	>90%
$(Fe_{2.2}Mn_{0.8})_{1-\delta}O_4$	Q	2.86	3.20	4.44	5.10	1.04	<0.3	<0.3
	η	56%	56%	7%	7%	89%	>90%	>90%
$(Fe_2Ti_{0.8}Mn_{0.2})_{1-\delta}O_4$	Q	2.21	3.67	4.42	3.32	2.84	1.10	1.76
	η	74%	36%	61%	69%	84%	73%	69%
$(Fe_2Ti_{0.5}Mn_{0.5})_{1-\delta}O_4$	Q	2.50	4.39	3.86	3.72	3.96	4.04	1.82
	η	42%	2%	39%	55%	9%	14%	86%
$(Fe_2Ti_{0.3}Mn_{0.7})_{1-\delta}O_4$	Q	3.59	4.66	3.10	4.54	4.34	2.18	1.58
	η	44%	65%	77%	15%	71%	>90%	82%
$(Fe_2Ni_{0.2}Mn_{0.8})_{1-\delta}O_4$	Q	1.04	1.21	0.92	1.27	0.47	<0.3	<0.3
	η	73%	79%	71%	82%	>90%	>90%	>90%

by the magnetic catalyst. The amount of elemental mercury captured per unit mass of catalyst (capacity) can be calculated from the breakthrough curve. Table 3 shows the capacities of synthesized magnetic catalysts for elemental mercury capture (Q) and the breakthrough ratios (the ratio of the outlet concentration of elemental mercury to the inlet concentration of elemental mercury at 10 h, η) as a function of reaction temperature under air.

As shown in Table 3, $(Fe_2Ti_{03}Mn_{0.7})_{1-\delta}O_4$, $(Fe_2Ti_{0.5}Mn_{0.5})_{1-\delta}O_4$ and $(Fe_2Ti_{0.8}Mn_{0.2})_{1-\delta}O_4$ showed excellent capacities for elemental mercury capture, especially at 150–300 °C. In comparison with $(Fe_{2.2}Mn_{0.8})_{1-\delta}O_4$, $(Fe_2Ti_{0.3}Mn_{0.7})_{1-\delta}O_4$ showed higher capacities for elemental mercury capture except at 200–250 °C. The capacities of $(Fe_2Ti_{0.8}Mn_{0.2})_{1-\delta}O_4$ and $(Fe_2Ti_{0.5}Mn_{0.5})_{1-\delta}O_4$ for elemental mercury capture were generally much more than those of $(Fe_{2.8}Mn_{0.2})_{1-\delta}O_4$ and $(Fe_{2.5}Mn_{0.5})_{1-\delta}O_4$, respectively. Especially, the capacity of $(Fe_2Ti_{0.8}Mn_{0.2})_{1-\delta}O_4$ for elemental mercury capture was generally much more than the sum of $(Fe_{2.8}Mn_{0.2})_{1-\delta}O_4$ and $(Fe_{2.2}Ti_{0.8})_{1-\delta}O_4$ except at 250 °C. At >250 °C, the capacity of $(Fe_2Ti_xMn_{1-x})_{1-\delta}O_4$ for elemental mercury capture was much more than that of $(Fe_{3-x}Mn_x)_{1-\delta}O_4$. All of those indicate that elemental mercury capture by Mn–Fe spinel was generally promoted due to the introduction of Ti. However, the incorporation of Ni into Mn–Fe spinel showed an obvious negative effect on elemental mercury capture (shown in Table 3).

3.2.2. Mechanism for elemental mercury capture

Elemental mercury oxidization by metal oxides in the absence of halogen may be attributed to the Mars–Maessen mechanism [2,15,23]. The possible reactions are as follows:

$$Hg^0_{(g)} + \equiv \square \rightarrow \equiv \square - Hg^0_{(ad)} \quad (3)$$

$$\equiv Mn^{IV} + 2 \equiv \square - Hg^0_{(ad)} + \equiv O \rightarrow \equiv Mn^{II} + Hg^I_2O_{(ad)} \quad (4)$$

$$\equiv Mn^{IV} + \equiv \square - Hg^0_{(ad)} + \frac{1}{2} \equiv O \rightarrow \equiv Mn^{III} + \frac{1}{2}Hg^I_2O_{(ad)} \quad (5)$$

$$\equiv Fe^{III} + \equiv \square - Hg^0_{(ad)} + \frac{1}{2} \equiv O \rightarrow \equiv Fe^{II} + \frac{1}{2}Hg^I_2O_{(ad)} \quad (6)$$

$$2 \equiv Mn^{IV} + \equiv \square - Hg^0_{(ad)} + \equiv O \rightarrow 2 \equiv Mn^{III} + Hg^{II}O_{(ad)} \quad (7)$$

$$\equiv Mn^{IV} + \equiv \square - Hg^0_{(ad)} + \equiv O \rightarrow \equiv Mn^{II} + Hg^{II}O_{(ad)} \quad (8)$$

$$\equiv Mn^{II} + \frac{1}{2}O_{2(g)} \rightarrow \equiv Mn^{IV} + \equiv O \quad (9)$$

$$\equiv Mn^{III} + \frac{1}{4}O_{2(g)} \rightarrow \equiv Mn^{IV} + \frac{1}{2} \equiv O \quad (10)$$

$$\equiv Fe^{II} + \frac{1}{4}O_{2(g)} \rightarrow \equiv Fe^{III} + \frac{1}{2} \equiv O \quad (11)$$

Reaction (3) was the collision of elemental mercury with the surface, resulting in a physical adsorption on the cation vacancies. If the concentration of elemental mercury in the gas phase was sufficiently high for the surface to be saturated with physically adsorbed elemental mercury, the concentration of physically adsorbed elemental mercury on the surface ($[\equiv \square - Hg^0_{(ad)}]$) can be described as:

$$[\equiv \square - Hg^0_{(ad)}] = k_1[\equiv \square] \quad (12)$$

where $[\equiv \square]$ and k_1 were the percent of cation vacancies on the surface and the constant, respectively.

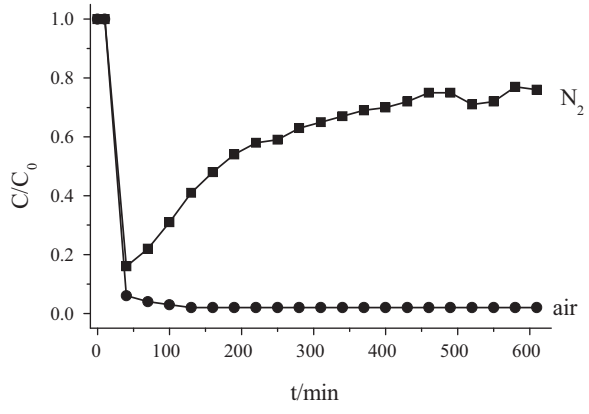

Fig. 6. Breakthrough curves of elemental mercury capture by $(Fe_2Ti_{0.5}Mn_{0.5})_{1-\delta}O_4$ at 250 °C under air and N_2.

Table 4
Numbers of cation vacancies and Mn^{4+} cations on synthesized samples.

	δ	Number of cation vacancies on the surface[a] ($m^2\ g^{-1}$)	Number of Mn^{4+} cations on the surface ($m^2\ g^{-1}$)
$(Fe_{2.8}Mn_{0.2})_{1-\delta}O_4$	0.11	3.9	1.3
$(Fe_{2.5}Mn_{0.5})_{1-\delta}O_4$	0.15	4.5	4.2
$(Fe_{2.2}Mn_{0.8})_{1-\delta}O_4$	0.19	3.1	4.3
$(Fe_2Ti_{0.8}Mn_{0.2})_{1-\delta}O_4$	0.19	4.6	1.0
$(Fe_2Ti_{0.5}Mn_{0.5})_{1-\delta}O_4$	0.16	7.4	3.4
$(Fe_2Ti_{0.3}Mn_{0.7})_{1-\delta}O_4$	0.15	3.4	2.6
$(Fe_2Ni_{0.2}Mn_{0.8})_{1-\delta}O_4$	0.12	2.6	2.7

[a] BET surface areas of $(Fe_{2.8}Mn_{0.2})_{1-\delta}O_4$, $(Fe_{2.5}Mn_{0.5})_{1-\delta}O_4$, $(Fe_{2.2}Mn_{0.8})_{1-\delta}O_4$ and $(Fe_2Ni_{0.2}Mn_{0.8})_{1-\delta}O_4$ were 82.9, 69.4, 37.8 and 50.4 $m^2\ g^{-1}$, respectively.

As shown in Eq. (12), the concentration of elemental mercury physically adsorbed was proportional to the percent of cation vacancies on the surface. In Table 4, the number of cation vacancies on $(Fe_2Ti_xMn_{1-x})_{1-\delta}\square_{3\delta}O_4$ was described as the product of BET surface area and $3\delta/7$ (the percent of cation vacancies on the surface). Reaction (3) was an exothermic reaction, so the constant k_1 would decrease with the increase of reaction temperature. Reactions (4)–(8) were the possible routes for the oxidation of physically adsorbed elemental mercury. Fig. 6 shows that elemental mercury capture by $(Fe_2Ti_{0.5}Mn_{0.5})_{1-\delta}O_4$ under air was much better than that under N_2. It indicates that the re-oxidization of formed Mn^{3+}, Mn^{2+} and Fe^{2+} cations (Reactions (9)–(11)) happened. During the re-oxidization, some cation vacancies may be recovered.

Our previous researches demonstrated that elemental mercury oxidization by $(Fe_{2.2}Mn_{0.8})_{1-\delta}O_4$ followed Reactions (4) or (5), and elemental mercury oxidization by $(Fe_2Ti)_{1-\delta}O_4$ followed Reaction (6). As shown in Table 3, Reaction (6) did not happen at <200 °C.

The specific mechanism for elemental mercury capture by $(Fe_2Ti_xMn_{1-x})_{1-\delta}O_4$ was studied using XPS analysis. In comparison with fresh $(Fe_2Ti_xMn_{1-x})_{1-\delta}O_4$, no obvious changes happened in the XPS spectra over the spectral regions of Ti 2p, Fe 2p and O 1s (the spectra was not shown). Taking account of the binding energy of Hg $4f_{7/2}$ at 100.1 eV and the absence of Hg $4f_{5/2}$ at about 105 eV corresponding to Hg^{2+} (shown in Fig. 7a), the oxidized mercury formed during the capture by $(Fe_2Ti_{0.8}Mn_{0.2})_{1-\delta}O_4$ may be mercurous oxide (Hg_2O). Thus, elemental mercury capture by $(Fe_2Ti_{0.8}Mn_{0.2})_{1-\delta}O_4$ followed Reactions (4) or (5). This was consistent with elemental mercury capture by $(Fe_{2.2}Mn_{0.8})_{1-\delta}O_4$.

As is well known, mercury is a heavy metal and its atomic radius (1.76 Å) is much bigger than the radiuses of Mn^{4+} (0.60 Å), Mn^{3+} (0.66 Å), Mn^{2+} (0.80 Å), Fe^{3+} (0.64 Å), Ti^{4+} (0.68 Å) and O^{2-} (1.32 Å). When a mercury atom is physically adsorbed on the cation vacancy, several ions including Mn^{4+}, Mn^{3+}, Mn^{2+}, Ti^{4+}, Fe^{3+} and O^{2-} around the cation vacancy may be covered. Once the adsorbed elemental mercury contacts Mn^{4+} cation on the surface, the adsorbed elemental mercury will be oxidized.

The array of cation vacancies, $Mn^{2+}/Mn^{3+}/Mn^{4+}$, Fe^{3+}, Ti^{4+} and O^{2-} in/on $(Fe_2Ti_xMn_{1-x})_{1-\delta}O_4$ was well-proportioned even at the atomic scale due to the incorporation of Ti and Mn cations into the spinel structure. On $(Fe_2Ti_xMn_{1-x})_{1-\delta}O_4$, the near two Mn cations were spaced by at least 2 Fe cations and 4 oxygen anions, so the distance between two Mn cations was much more than the diameter of the Hg atom. When a mercury atom was physically adsorbed on the active site (i.e. □), at most one Mn^{4+} cation can be covered, so Reaction (7) cannot happen in this case. Meanwhile, the distance between Mn^{4+} and the nearest Fe^{3+} was less than the diameter of the Hg atom.

Because all Mn^{4+} cations on the surface resulted from the oxidization of Mn^{2+} cations, there was a Mn^{4+} cation around each cation vacancy resulting from the oxidization of Mn^{2+}. Most of the cation vacancies on $(Fe_{2.2}Mn_{0.8})_{1-\delta}O_4$ resulted from the oxidization of Mn^{2+} to Mn^{4+}/Mn^{3+} cations, but about 41% and 83% of the cation vacancies on $(Fe_{2.5}Mn_{0.5})_{1-\delta}O_4$ and $(Fe_{2.8}Mn_{0.2})_{1-\delta}O_4$ resulted from the oxidization of Fe^{2+} cations. Furthermore, only about 20% and 29% of the Fe^{3+} cations on $(Fe_{2.5}Mn_{0.5})_{1-\delta}O_4$ and $(Fe_{2.8}Mn_{0.2})_{1-\delta}O_4$ involved cation vacancies, respectively. Thus, the probability of the collision between elemental mercury adsorbed on the cation vacancies resulting from the oxidization of Fe^{2+} cations and Mn^{4+} cations on the surface was small, so a large amount of these cation vacancies had no contribution to elemental mercury oxidization. As a result, the capacity of $(Fe_{2.5}Mn_{0.5})_{1-\delta}O_4$ for elemental mercury capture was less than that of $(Fe_{2.2}Mn_{0.8})_{1-\delta}O_4$ (shown in Table 3), although the number of cation vacancies on $(Fe_{2.5}Mn_{0.5})_{1-\delta}O_4$ was more than that on $(Fe_{2.2}Mn_{0.8})_{1-\delta}O_4$ and the number of Mn^{4+} cations on $(Fe_{2.5}Mn_{0.5})_{1-\delta}O_4$ was close to that on $(Fe_{2.2}Mn_{0.8})_{1-\delta}O_4$ (shown in Table 4).

With the incorporation of Ti into Mn–Fe spinel, both the cation vacancies resulting from the oxidization of Fe^{2+} cations and the Fe^{3+} cations involving cation vacancies obviously increased. About 87%, 63% and 43% of cation vacancies on $(Fe_2Ti_{0.8}Mn_{0.2})_{1-\delta}O_4$, $(Fe_2Ti_{0.5}Mn_{0.5})_{1-\delta}O_4$ and $(Fe_2Ti_{0.3}Mn_{0.7})_{1-\delta}O_4$ resulted from the oxidization of Fe^{2+} cations, respectively. And about 82%, 55% and 39% of Fe^{3+} cations on $(Fe_2Ti_{0.8}Mn_{0.2})_{1-\delta}O_4$, $(Fe_2Ti_{0.5}Mn_{0.5})_{1-\delta}O_4$ and $(Fe_2Ti_{0.3}Mn_{0.7})_{1-\delta}O_4$ involved cation vacancies, respectively. As a result, the probability of elemental mercury adsorbed on the cation vacancies resulting from the oxidization of Fe^{2+} cations contacting Mn^{4+} cations on the surface obviously increased with the increase of Ti content. Therefore, elemental mercury capture by $(Fe_{3-x}Mn_x)_{1-\delta}O_4$ was generally promoted due to the incorporation of Ti.

Most of the elemental mercury adsorbed on the cation vacancies on $(Fe_2Ti_{0.8}Mn_{0.2})_{1-\delta}O_4$ can contact Mn^{4+} cations on the surface whether the cation vacancies resulted from the oxidization of Fe^{2+} cations or Mn^{2+} cations. Furthermore, the number of cation vacancies (corresponding to elemental mercury physically adsorbed) was 4.6 times that of Mn^{4+} cations on $(Fe_2Ti_{0.8}Mn_{0.2})_{1-\delta}O_4$ (shown in Table 4). As a result, elemental mercury capture by $(Fe_2Ti_{0.8}Mn_{0.2})_{1-\delta}O_4$ may mainly follow Reaction (4). However, the number of cation vacancies was slightly less than that of Mn^{4+} cations on $(Fe_{2.2}Mn_{0.8})_{1-\delta}O_4$ (shown in Table 4), so elemental mercury capture by $(Fe_{2.2}Mn_{0.8})_{1-\delta}O_4$ may mainly follow Reaction (5). Because Mn^{4+} cation may be reduced by □ to Mn^{3+} cation at higher temperatures [44], $(Fe_{3-x}Mn_x)_{1-\delta}O_4$ showed poor capacity for elemental mercury capture at >300 °C. Because both the number of cation vacancies and the number of Mn^{4+} cations on the surface decreased due to the incorporation of Ni into the structure of Mn–Fe spinel (shown in Table 4), the capacity of $(Fe_2Ni_{0.2}Mn_{0.8})_{1-\delta}O_4$ for elemental mercury capture was much less than that of $(Fe_{2.2}Mn_{0.8})_{1-\delta}O_4$.

XPS spectrum of $(Fe_2Ti_{0.5}Mn_{0.5})_{1-\delta}O_4$ after elemental mercury capture over Hg 4f spectral region is shown in Fig. 7b. Taking account of the binding energies of Hg $4f_{7/2}$ at 101.3 eV and Hg $4f_{5/2}$ at about 105.5 eV (the binding energy centered at about 103.8 eV was attributed to Si 2p of SiO_2 in quartz wool), the oxidized mercury formed was mercuric oxide (HgO). This indicates that elemental mercury capture by $(Fe_2Ti_{0.5}Mn_{0.5})_{1-\delta}O_4$ mainly followed Reaction (8). There were a large number of cation vacancies

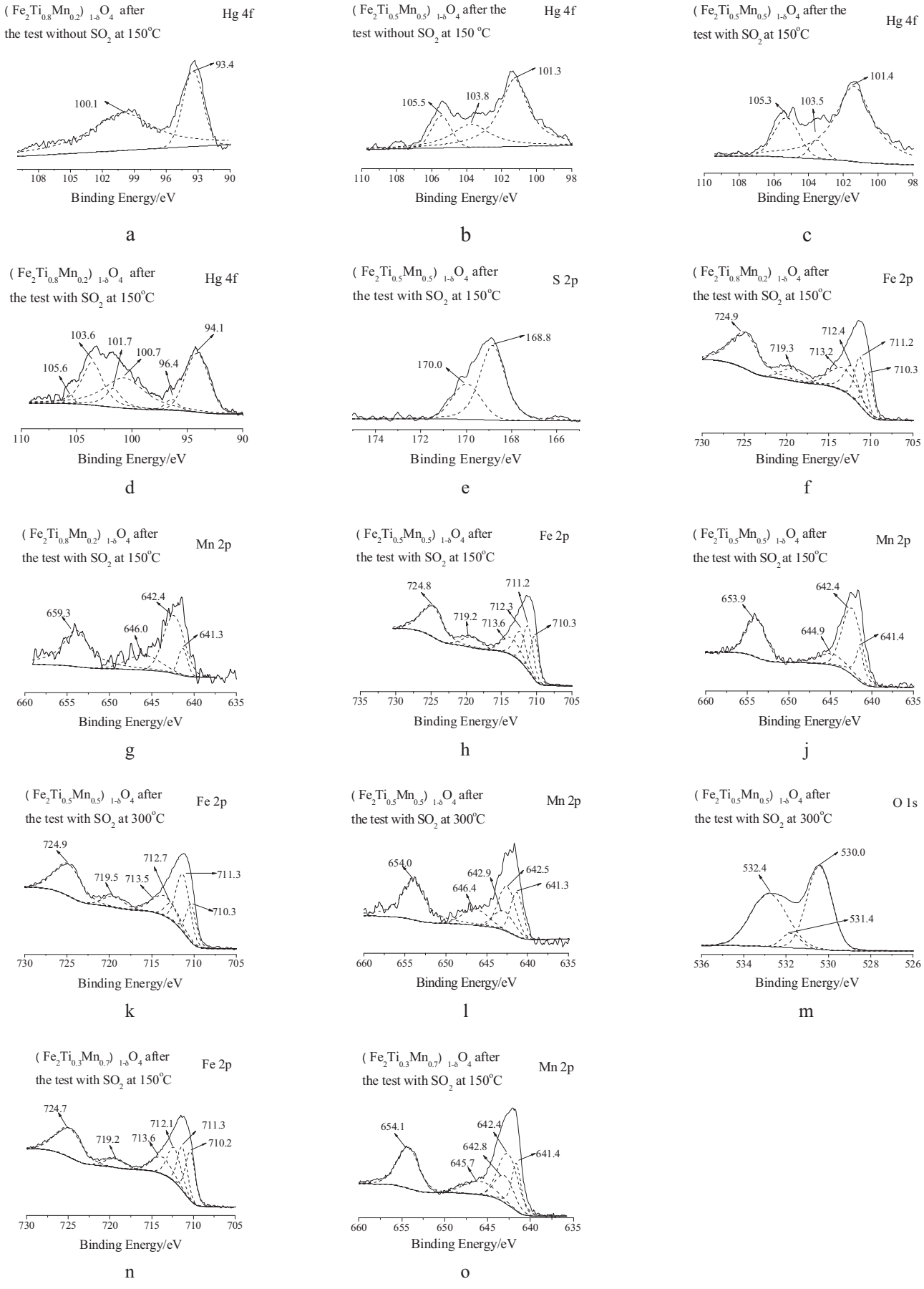

Fig. 7. XPS spectra of synthesized samples after the test over the spectral regions of Fe 2p, Mn 2p, Hg 4f, S 2p and O 1s.

Table 5
Capacity (Q) and breakthrough ratio (η) of synthesized samples for elemental mercury capture in the presence of a high concentration of SO_2 ($mg\,g^{-1}$).

		100 °C	150 °C	200 °C	250 °C	300 °C	350 °C	400 °C
$(Fe_2Ti)_{1-\delta}O_4$	Q	<0.3	<0.3	0.46	1.00	0.42	0.36	<0.3
	η	>90%	>90%	47%	80%	>90%	>90%	>90%
$(Fe_{2.2}Mn_{0.8})_{1-\delta}O_4$	Q	2.38	1.92	1.72	2.48	0.96	<0.3	<0.3
	η	82%	86%	90%	70%	82%	>90%	>90%
$(Fe_2Ti_{0.8}Mn_{0.2})_{1-\delta}O_4$	Q	1.19	1.53	1.64	1.68	0.97	0.44	<0.3
	η	84%	90%	85%	87%	86%	>90%	>90%
$(Fe_2Ti_{0.5}Mn_{0.5})_{1-\delta}O_4$	Q	3.00	4.17	1.53	1.99	1.41	1.37	2.06
	η	43%	23%	90%	75%	77%	83%	82%
$(Fe_2Ti_{0.3}Mn_{0.7})_{1-\delta}O_4$	Q	2.65	2.63	2.40	2.84	1.24	0.48	<0.3
	η	30%	46%	47%	89%	84%	>90%	>90%

on $(Fe_2Ti_{0.5}Mn_{0.5})_{1-\delta}O_4$ (shown in Table 4) and the concentration of elemental mercury may not be sufficiently high in the gas phase for the surface to be saturated with physically adsorbed elemental mercury. Some cation vacancies were vacant for the physical adsorption of elemental mercury and there may at most be one mercury atom physically adsorbed around every Mn^{4+} cation. As a result, Reaction (8) occurred.

Although Reactions (4)–(11) were promoted with the increase of reaction temperature, elemental mercury capture reached the optimal condition at a specific temperature, in most case not the highest temperature due to the influence of reaction temperature on the physical adsorption (Reaction (3)).

3.3. Effect of SO_2 on elemental mercury capture

The capacities of $(Fe_2Ti_xMn_{1-x})_{1-\delta}O_4$ for elemental mercury capture in the presence of 1000 ppm of SO_2 are shown in Table 5. Elemental mercury capture by $(Fe_2Ti_{0.8}Mn_{0.2})_{1-\delta}O_4$ was significantly influenced by a high concentration of SO_2. The presence of a high concentration of SO_2 resulted in an insignificant effect on elemental mercury capture by $(Fe_2Ti_{0.5}Mn_{0.5})_{1-\delta}O_4$ at 100–150 °C, but it showed an obvious interference at 200–350 °C. The presence of a high concentration of SO_2 resulted in a moderate effect on elemental mercury capture by $(Fe_2Ti_{0.3}Mn_{0.7})_{1-\delta}O_4$ at 100–250 °C, but it showed a serious interference at 300–400 °C. The capacity of $(Fe_2Ti_{0.3}Mn_{0.7})_{1-\delta}O_4$ for elemental mercury capture in the presence of SO_2 was more than that of $(Fe_{2.2}Mn_{0.8})_{1-\delta}O_4$. This indicates that the incorporation of Ti may promote elemental mercury capture by Mn–Fe spinel in the presence of a high concentration of SO_2.

Previous research postulated a mechanism for the heterogeneous uptake and oxidization of SO_2 on iron oxides [30], and the reactions can be described as:

$$\equiv Fe^{III}\text{–}OH + SO_{2(g)} \rightarrow \equiv Fe^{III}OSO_2^- + H^+ \quad (13)$$

$$\equiv Fe^{III}OSO_2^- \rightarrow \equiv Fe^{II} + SO_3^{\bullet -} \quad (14)$$

$$\equiv Fe^{III}\text{–}OH + SO_3^{\bullet -} \rightarrow \equiv Fe^{II}\text{–}SO_4^{2-} + H^+ \quad (15)$$

As shown in Reactions (13)–(15), the uptake of SO_2 on iron oxides may involve hydroxyl groups on the surface. In the absence of hydroxyl groups, the uptake of SO_2 on iron oxides can be neglected [30]. Furthermore, SO_2 can also react with Mn^{4+} cations on the surface [31] and the reaction can be described as:

$$SO_{2(g)} + \equiv Mn^{IV} + 2 \equiv O \rightarrow \equiv Mn^{II}\text{–}SO_4 \quad (16)$$

Reactions (13)–(16) may happen during elemental mercury capture by $(Fe_2Ti_xMn_{1-x})_{1-\delta}O_4$ in the presence of SO_2, resulting in an interference with elemental mercury capture.

The effect of a high concentration of SO_2 on elemental mercury capture by $(Fe_2Ti_xMn_{1-x})_{1-\delta}O_4$ was studied using XPS analysis (shown in Fig. 7). The Hg 4f peaks for $(Fe_2Ti_{0.5}Mn_{0.5})_{1-\delta}O_4$ after the test with SO_2 still centered at about 101.4 and 105.3 eV (shown in Fig. 7c). This indicates that the oxidized mercury formed was still HgO in the presence of a high concentration of SO_2. However, the Hg 4f peak for $(Fe_2Ti_{0.8}Mn_{0.2})_{1-\delta}O_4$ after the test with SO_2 mainly transformed to 100.7 eV (shown in Fig. 7d). This indicates that the oxidized mercury may transform to Hg_2SO_4 in the presence of a high concentration of SO_2. It is noted that mercurous sulfate has been previously observed as a mercury product in a photochemical oxidation process for elemental mercury oxidation and capture [12,13]. XPS spectra demonstrated the formation of SO_4^{2-} during elemental mercury capture. The S 2p peaks mainly centered at about 168.8 and 170.0 eV (shown in Fig. 7e), which may be assigned to SO_4^{2-} and HSO_4^-, respectively. The formation of sulfate can also be supported by the XPS spectra over Fe 2p, Mn 2p and O 1s regions. The peaks centered at about 713.5, 642.8 and 532.4 eV, may be assigned to Fe $2p_{3/2}$ of $Fe_2(SO_4)_3$, Mn $2p_{3/2}$ of $MnSO_4$ and O 1s of SO_4^{2-}, respectively (shown in Fig. 7f–o). During elemental mercury capture by $(Fe_2Ti_xMn_{1-x})_{1-\delta}O_4$ in the presence of SO_2, the percent of $\equiv Fe^{III}$–OH obviously decreased with the formation of $Fe_2(SO_4)_3$, which was consistent with the postulated mechanism that the uptake of SO_2 on iron oxides involved $\equiv Fe^{III}$–OH [31].

The peak centered at about 642.8 eV corresponding to $MnSO_4$ did not appear in the XPS spectra of $(Fe_2Ti_{0.8}Mn_{0.2})_{1-\delta}O_4$ and $(Fe_2Ti_{0.5}Mn_{0.5})_{1-\delta}O_4$ after the test at 150 °C in the presence of SO_2 (shown in Fig. 7g and j). As shown in Table 2, the number of $\equiv Fe^{III}$–OH was much greater than the number of Mn^{4+} cations on $(Fe_2Ti_{0.8}Mn_{0.2})_{1-\delta}O_4$ and $(Fe_2Ti_{0.5}Mn_{0.5})_{1-\delta}O_4$, so SO_2 mainly reacted with $\equiv Fe^{III}$–OH on the surface, and few Mn^{4+} cations reacted with SO_2. XPS analysis showed that 31% and 20% of Fe^{3+} cations on $(Fe_2Ti_{0.8}Mn_{0.2})_{1-\delta}O_4$ and $(Fe_2Ti_{0.5}Mn_{0.5})_{1-\delta}O_4$ were sulfated, respectively. Once ferric sulfate formed, the corresponding cation vacancies would be destroyed and they can not be regenerated. 100% and 82% of Fe^{3+} cations on $(Fe_2Ti)_{1-\delta}O_4$ and $(Fe_2Ti_{0.8}Mn_{0.2})_{1-\delta}O_4$ involved cation vacancies, respectively, so a serious destruction of cation vacancies occurred during the reaction of SO_2 with $\equiv Fe^{III}$–OH. As a result, the presence of a high concentration of SO_2 resulted in severe interference with elemental mercury capture by $(Fe_2Ti)_{1-\delta}O_4$ and $(Fe_2Ti_{0.8}Mn_{0.2})_{1-\delta}O_4$.

55% of the Fe^{3+} cations on $(Fe_2Ti_{0.5}Mn_{0.5})_{1-\delta}O_4$ involved cation vacancies. Some of the involved cation vacancies may have no contribution for elemental mercury oxidization because Mn^{4+} cations on the surface were far away from them. Furthermore, the number of cation vacancies on $(Fe_2Ti_{0.5}Mn_{0.5})_{1-\delta}O_4$ may be superfluous for the saturated physical adsorption of elemental mercury. Thus, the moderate decrease of cation vacancies due to the presence of a high concentration of SO_2 resulted in an insignificant effect on elemental mercury capture by $(Fe_2Ti_{0.5}Mn_{0.5})_{1-\delta}O_4$ at lower temperatures (100–150 °C). With the increase of reaction temperature, the amount of $\equiv Fe^{III}$–OH would decrease due to the dehydration. As a result, $MnSO_4$ appeared in the XPS spectra of $(Fe_2Ti_{0.5}Mn_{0.5})_{1-\delta}O_4$

Table 6
Comparison of the performance of $(Fe_2Ti_{0.5}Mn_{0.5})_{1-\delta}O_4$ with other catalysts/sorbents.

Catalyst/sorbent	Capacity/mg g^{-1}	Carrier gas	Temperature/°C	Magnetization/emu g^{-1}
I-AC [53]	0.85	Air	140	–
DARCO Hg-LH [54]	8.9	Air	140	–
S-AC [55]	1.9	Simulated fuel gas	140	–
Cl-AC [23]	4.0	Ar	138	–
V_2O_5/TiO_2 [48]	0.23	Air	100	–
MnO_2/Al_2O_3 [23]	3.5	Air	138	–
Z-Ag^0 [56]	0.5	Ar	150	–
Pd/Al_2O_3 [57]	0.9	Simulated fuel gas	288	–
MagZ-Ag^0 [25,32]	0.044	Ar	150	40
$(Fe_2Ti_{0.5}Mn_{0.5})_{1-\delta}O_4$	4.2	Air with SO_2	150	31

after the test with SO_2 at 300 °C (shown in Fig. 7l). Furthermore, the reaction rate constants of Reactions (13)–(16) may increase with the increase of reaction temperature. XPS analysis showed that 28% of Fe^{3+} cations and 24% of Mn cations were sulfated. Because both the number of Mn^{4+} cations and the number of usable cation vacancies decreased, elemental mercury capture by $(Fe_2Ti_{0.5}Mn_{0.5})_{1-\delta}O_4$ was obviously interfered by the high concentration of SO_2 at high temperatures.

With the increase of Mn^{4+} cations on the surface, both $Fe_2(SO_4)_3$ and $MnSO_4$ appeared in the XPS spectra of $(Fe_2Ti_{0.3}Mn_{0.7})_{1-\delta}O_4$ after the test with SO_2 at 150 °C (shown in Fig. 7n and o). As a result, elemental mercury capture by $(Fe_2Ti_{0.3}Mn_{0.7})_{1-\delta}O_4$ was obviously interfered by the high concentration of SO_2.

3.4. Comparison of $(Fe_2Ti_{0.5}Mn_{0.5})_{1-\delta}O_4$ with other catalysts/sorbents

Table 6 compares the performance of $(Fe_2Ti_{0.5}Mn_{0.5})_{1-\delta}O_4$ for elemental mercury capture with those of other catalysts/sorbents.

Pretreated powdered activated carbon (I-AC, Br-AC, S-AC and Cl-AC) showed excellent capacities for elemental mercury capture. Direct injection of pretreated powdered activated carbon into the flue gas upstream of a particulate collector is currently considered the maximum available control technology for the removal of elemental mercury from the flue gas in coal-fired utilities, since almost all coal-fired power plants are equipped with an electrostatic precipitator or a baghouse [46,47]. However, the separation of powdered activated carbon from the fly ash was extremely difficult and impractical. The fly ash with a large amount of activated carbon cannot be directly used. Furthermore, the fly ash would be contaminated by the formed mercury product.

SCR catalysts are mainly employed to reduce NO_x concentration in the flue gas, and elemental mercury may be removed as a cobenefit. The catalyst is typically composed of vanadium pentoxide (V_2O_5) supported on titanium dioxide (TiO_2). Laboratory-scale tests verify that SCR can oxidize Hg^0 to Hg^{2+}, particularly in the presence of HCl [18,48]. But in the absence of HCl, the capacity of supported V_2O_5 for elemental mercury capture is very poor. Furthermore, the injection of ammonia for the necessary NO_x control is a severe interferent for elemental mercury capture [49–51].

Development of metal and metal oxide catalysts can be used as an alternative [52]. Some metals and metal oxides showed excellent capacities for elemental mercury capture (for example MnO_2/Al_2O_3, Z-Ag^0 and Pd/Al_2O_3). However, the separation of the catalyst from the fly ash was still difficult. The separation of the catalyst from the fly ash can be achieved by the magnetic property of the catalyst. A magnetic MagZ-Ag^0 was once developed to capture elemental mercury [25,32]. However, its capacity for elemental mercury capture was very poor, and its cost was expensive due to the use of noble metal Ag. Here, magnetic $(Fe_2Ti_xMn_{1-x})_{1-\delta}O_4$ was developed for elemental mercury capture. Because the temperature of the flue gas after the air preheater (APH) or before the electrostatic precipitator is about 150 °C, it is the workable temperature for elemental mercury capture by a catalyst. $(Fe_2Ti_{0.5}Mn_{0.5})_{1-\delta}O_4$ showed an excellent capacity for elemental mercury capture (>4.2 mg g^{-1}) at about 150 °C in the presence of a high concentration of SO_2. The catalyst can be separated from the fly ash mixture using magnetic separation, which makes them possible to use the catalyst multiple times and regenerate the catalyst. Furthermore, the adsorbed mercury product may be safely disposed during the regeneration of $(Fe_2Ti_{0.5}Mn_{0.5})_{1-\delta}O_4$.

4. Conclusions

A series of nanosized $(Fe_2Ti_{1-x}Mn_x)_{1-\delta}O_4$ were synthesized using a co-precipitation method to capture elemental mercury from the flue gas. Elemental mercury capture by non-stoichiometric Mn–Fe spinel depended on the number of Mn^{4+} cations (the oxidizing agent for elemental mercury oxidization) and the number of usable cation vacancies (the active site for the physical adsorption of elemental mercury) on the surface. Although the incorporation of Ti into Mn–Fe spinel suppressed the enrichment of Mn^{4+} cations on the surface, the number of usable cation vacancies obviously increased. As a result, the capacities of $(Fe_2Ti_{0.8}Mn_{0.2})_{1-\delta}O_4$ and $(Fe_2Ti_{0.5}Mn_{0.5})_{1-\delta}O_4$ for elemental mercury capture were generally much greater than those of $(Fe_{2.8}Mn_{0.2})_{1-\delta}O_4$ and $(Fe_{2.5}Mn_{0.5})_{1-\delta}O_4$, and the capacity of $(Fe_2Ti_{0.3}Mn_{0.7})_{1-\delta}O_4$ was greater than that of $(Fe_{2.2}Mn_{0.8})_{1-\delta}O_4$ except at 200–250 °C. Furthermore, the incorporation of Ti improved the SO_2 poisoning resistance of Mn–Fe spinel for elemental mercury capture. Especially, $(Fe_2Ti_{0.5}Mn_{0.5})_{1-\delta}O_4$ showed an excellent capacity (>4.2 mg g^{-1}) for elemental mercury capture in the presence of a high concentration of SO_2 at a workable temperature (about 150 °C). Meanwhile, $(Fe_2Ti_{0.5}Mn_{0.5})_{1-\delta}O_4$ can be easily separated from the fly ash due to its inherent magnetization. Both results indicate that $(Fe_2Ti_{0.5}Mn_{0.5})_{1-\delta}O_4$ may be a promising catalyst for the control of elemental mercury emission. In our future work, $(Fe_2Ti_{0.5}Mn_{0.5})_{1-\delta}O_4$ will be investigated to capture elemental mercury from the flue gas at a pilot scale, in which the influence of O_2, SO_2, CO, NO_x, HCl, NH_3 and H_2O, the separation of catalyst from the fly ash and catalyst regeneration will be further studied.

Acknowledgements

This study was supported by the High-Tech R&D Program of China (No. 2007AA06Z340) and Shanghai Tongji Gao Tingyao Environmental Science & Technology Development Foundation.

References

[1] D.G. Streets, J.M. Hao, Y. Wu, J.K. Jiang, M. Chan, H.Z. Tian, X.B. Feng, Atmos. Environ. 39 (2005) 7789–7806.
[2] A.A. Presto, E.J. Granite, Environ. Sci. Technol. 40 (2006) 5601–5609.
[3] C.E. Romero, Y. Li, H. Bilirgen, N. Sarunac, E.K. Levy, Fuel 85 (2006) 204–212.
[4] N.Q. Yan, Z. Qu, Y. Chi, S.H. Qiao, R.L. Dod, S.G. Chang, C. Miller, Environ. Sci. Technol. 43 (2009) 5410–5415.

[5] L. Ji, P.M. Sreekanth, P.G. Smirniotis, S.W. Thiel, N.G. Pinto, Energy Fuels 22 (2008) 2299–2306.
[6] D.Y. Lu, D.L. Granatstein, D.J. Rose, Ind. Eng. Chem. Res. 43 (2004) 5400–5404.
[7] S.X. Wang, L. Zhang, G.H. Li, Y. Wu, J.M. Hao, N. Pirrone, F. Sprovieri, M.P. Ancora, Atmos. Chem. Phys. 10 (2010) 1183–1192.
[8] M.H. Kim, S.-W. Ham, J.-B. Lee, Appl. Catal. B: Environ. 99 (2010) 272–278.
[9] Z.J. Mei, Z.M. Shen, Z.Y. Mei, Y. Zhang, F. Xiang, J.P. Chen, W.H. Wang, Appl. Catal. B: Environ. 78 (2008) 112–119.
[10] S. Straube, T. Hahn, H. Koeser, Appl. Catal. B: Environ. 79 (2008) 286–295.
[11] E.J. Granite, M.C. Freeman, R.A. Hargis, W.J. O'Dowd, H.W. Pennline, J. Environ. Manage. 84 (2007) 628–634.
[12] C.R. McLarnon, E.J. Granite, H.W. Pennline, Fuel Process. Technol. 87 (2005) 85–89.
[13] E.J. Granite, H.W. Pennline, Ind. Eng. Chem. Res. 41 (2002) 5470–5476.
[14] W.J. O'Dowd, H.W. Pennline, M.C. Freeman, E.J. Granite, R.A. Hargis, C.J. Lacher, A. Karash, Fuel Process. Technol. 87 (2006) 1071–1084.
[15] A.A. Presto, E.J. Granite, Platinum Met. Rev. 52 (2008) 144–154.
[16] Y. Li, P. Murphy, C.Y. Wua, Fuel Process. Technol. 89 (2008) 567–573.
[17] Y. Li, C.Y. Wu, Environ. Sci. Technol. 40 (2006) 6444–6448.
[18] Y. Li, P.D. Murphy, C.Y. Wu, K.W. Powers, J.C.J. Bonzongo, Environ. Sci. Technol. 42 (2008) 5304–5309.
[19] A.A. Presto, E.J. Granite, A. Karash, R.A. Hargis, W.J. O'Dowd, H.W. Pennline, Energy Fuels 20 (2006) 1941–1945.
[20] E.J. Granite, W.P. King, D.C. Stanko, H.W. Pennline, Main Group Chem. 7 (2008) 227–237.
[21] E.J. Granite, H.W. Pennline, J.S. Hoffman, Ind. Eng. Chem. Res. 38 (1999) 5034–5037.
[22] C. Borderieux, C.Y. Wu, J.C. Bonzongo, K. Powers, Aerosol Air Qual. Res. 4 (2004) 74–90.
[23] E.J. Granite, H.W. Pennline, R.A. Hargis, Ind. Eng. Chem. Res. 39 (2000) 1020–1029.
[24] S. Yang, Y. Guo, N. Yan, D. Wu, H. He, J. Xie, Z. Qu, C. Yang, J. Jia, Chem. Commun. 46 (2010) 8377–8379.
[25] J. Dong, Z.H. Xu, S.M. Kuznicki, Adv. Funct. Mater. 19 (2009) 1268–1275.
[26] G.S. Qi, R.T. Yang, J. Catal. 217 (2003) 434–441.
[27] A.A. Presto, E.J. Granite, Environ. Sci. Technol. 41 (2007) 6579–6584.
[28] W.Q. Xu, H. He, Y.B. Yu, J. Phys. Chem. C 113 (2009) 4426–4432.
[29] A.A. Presto, E.J. Granite, A. Karash, Ind. Eng. Chem. Res. 46 (2007) 8273–8276.
[30] H.B. Fu, X. Wang, H.B. Wu, Y. Yin, J.M. Chen, J. Phys. Chem. C 111 (2007) 6077–6085.
[31] W.S. Kijlstra, M. Biervliet, E.K. Poels, A. Bliek, Appl. Catal. B: Environ. 16 (1998) 327–337.
[32] J. Dong, Z.H. Xu, S.M. Kuznicki, Environ. Sci. Technol. 43 (2009) 3266–3271.
[33] L.C.A. Oliveira, J.D. Fabris, R. Rios, W.N. Mussel, R.M. Lago, Appl. Catal. A: Gen. 259 (2004) 253–259.
[34] R.M. Cornell, U. Schwertmann, The Iron Oxides: Structure, Properties, Reactions, Occurrences and Uses, Wiley–VCH, New York, 2003.
[35] R.Q. Long, R.T. Yang, R. Chang, Chem. Commun. 5 (2002) 452–453.
[36] R.Q. Long, R.T. Yang, J. Catal. 207 (2002) 158–165.
[37] F.D. Liu, H. He, Y. Ding, C.B. Zhang, Appl. Catal. B: Environ. 93 (2009) 194–204.
[38] F. Liu, H. He, C. Zhang, Chem. Commun. 17 (2008) 2043–2045.
[39] F.D. Liu, H. He, C.B. Zhang, Z.C. Feng, L.R. Zheng, Y.N. Xie, T.D. Hu, Appl. Catal. B: Environ. 96 (2010) 408–420.
[40] S. Yang, H. He, D. Wu, D. Chen, X. Liang, Z. Qin, M. Fan, J. Zhu, P. Yuan, Appl. Catal. B: Environ. 89 (2009) 527–535.
[41] T. Herranz, S. Rojas, M. Ojeda, F.J. Perez-Alonso, P. Tefferos, K. Pirota, J.L.G. Fierro, Chem. Mater. 18 (2006) 2364–2375.
[42] Y. Zhang, M. Yang, X.M. Dou, H. He, D.S. Wang, Environ. Sci. Technol. 39 (2005) 7246–7253.
[43] B. Gillot, M. Laarj, S. Kacim, J. Mater. Chem. 7 (1997) 827–831.
[44] B. Gillot, V. Nivoix, E. Kester, O. Nusillard, C. Villette, P. Tailhades, A. Rousset, Mater. Chem. Phys. 48 (1997) 111–118.
[45] N. Guigue-Millot, Y. Champion, M.J. Hytch, F. Bernard, S. Begin-Colin, P. Perriat, J. Phys. Chem. B 105 (2001) 7125–7132.
[46] Z.J. Mei, Z.M. Shen, Q.J. Zhao, W.H. Wang, Y.J. Zhang, J. Hazard. Mater. 152 (2008) 721–729.
[47] J.H. Pavlish, E.A. Sondreal, M.D. Mann, E.S. Olson, K.C. Galbreath, D.L. Laudal, S.A. Benson, Fuel Process. Technol. 82 (2003) 89–165.
[48] W.J. Lee, G.N. Bae, Environ. Sci. Technol. 43 (2009) 1522–1527.
[49] C.W. Lee, S.D. Serre, Y. Zhao, S.J. Lee, J. Air Waste Manage. 58 (2008) 484–493.
[50] J.R. Strege, C.J. Zygarlicke, B.C. Folkedahl, D.P. McCollor, Fuel 87 (2008) 1341–1347.
[51] K. Schofield, Environ. Sci. Technol. 42 (2008) 9014–9030.
[52] Z.J. Mei, Z.M. Shen, W.H. Wang, Y.J. Zhang, Environ. Sci. Technol. 42 (2008) 590–595.
[53] S.F. Lee, Y.C. Seo, J. Jurng, T.G. Lee, Atmos. Environ. 38 (2004) 4887–4893.
[54] S.S. Lee, J.Y. Lee, T.C. Keener, Fuel Process. Technol. 90 (2009) 1314–1318.
[55] H.C. Hsi, M.J. Rood, M. Rostam-Abadi, S.G. Chen, R. Chang, Environ. Sci. Technol. 35 (2001) 2785–2791.
[56] Y. Liu, D.J.A. Kelly, H.Q. Yang, C.C.H. Lin, S.M. Kuznicki, Z.G. Xu, Environ. Sci. Technol. 42 (2008) 6205–6210.
[57] E.J. Granite, C.R. Myers, W.P. King, D.C. Stanko, H.W. Pennline, Ind. Eng. Chem. Res. 45 (2006) 4844–4848.